Lawrence Berkeley National Laboratory
Lawrence Berkeley National Laboratory

Title
Infrared birefringence imaging of residual stress and bulk defects in multicrystalline silicon

Permalink
https://escholarship.org/uc/item/90c8x2ms

Author
Ganapati, Vidya

Publication Date
2010-09-05

eScholarship.org Powered by the California Digital Library
University of California

Infrared birefringence imaging of residual stress and bulk defects in multicrystalline silicon

Vidya Ganapati,[1] Stephan Schoenfelder,[1,2,3] Sergio Castellanos,[1] Sebastian Oener,[4] Ringo Koepge,[2,3] Aaron Sampson,[1] Matthew A. Marcus,[5] Barry Lai,[6] Humphrey Morhenn,[4] Giso Hahn,[4] Joerg Bagdahn,[2] and Tonio Buonassisi[1,a)]

[1]*Massachusetts Institute of Technology, Cambridge, Massachusetts 02139, USA*
[2]*Fraunhofer Center for Silicon Photovoltaics CSP, 06120 Halle, Germany*
[3]*Fraunhofer Institute for Mechanics of Materials IWM, 06120 Halle, Germany*
[4]*University of Konstanz, 78457 Konstanz, Germany*
[5]*Advanced Light Source, Lawrence Berkeley National Laboratory, Berkeley, California 94720, USA*
[6]*Advanced Photon Source, Argonne National Laboratory, Argonne, Illinois 60439, USA*

(Received 24 May 2010; accepted 29 June 2010; published online 22 September 2010)

This manuscript concerns the application of infrared birefringence imaging (IBI) to quantify macroscopic and microscopic internal stresses in multicrystalline silicon (mc-Si) solar cell materials. We review progress to date, and advance four closely related topics. (1) We present a method to decouple macroscopic thermally-induced residual stresses and microscopic bulk defect related stresses. In contrast to previous reports, thermally-induced residual stresses in wafer-sized samples are generally found to be less than 5 MPa, while defect-related stresses can be several times larger. (2) We describe the unique IR birefringence signatures, including stress magnitudes and directions, of common microdefects in mc-Si solar cell materials including: β-SiC and β-Si_3N_4 microdefects, twin bands, nontwin grain boundaries, and dislocation bands. In certain defects, local stresses up to 40 MPa can be present. (3) We relate observed stresses to other topics of interest in solar cell manufacturing, including transition metal precipitation, wafer mechanical strength, and minority carrier lifetime. (4) We discuss the potential of IBI as a quality-control technique in industrial solar cell manufacturing.

I. INTRODUCTION

To first order, both solar cell manufacturing yield and conversion efficiency are inversely related to the cost of photovoltaic power (PV).[1] Significant resources have been invested toward improving efficiencies, resulting in sophisticated camera-based imaging techniques. Today, camera-based photoluminescence imaging,[2,3] electroluminescence imaging,[4,5] and lock-in thermography[6–8] can detect and characterize the distribution of efficiency loss mechanisms over full wafers with submillimeter precision, under certain conditions even predicting the performance of final devices from measurements on wafers.[9–12]

In comparison, our current understanding of solar cell breakage and strength behavior is rudimentary. The strength of wafers and cells is widely evaluated via bending tests and Weibull statistics,[13] using a continuum approach[14–17] that assumes spatially-invariant (homogeneous) material properties. Hence, the strength of wafers can be described by statistical parameters, but often the cause of breakage cannot be determined. Multicrystalline silicon (mc-Si) contains heterogeneous residual stress distributions, which are caused by thermal gradients during crystallization within confined geometries, as well as microdefect-related stresses. Since large internal stresses reduce the maximum external (applied) load a sample can withstand before fracture, the lack of ability to image internal stresses has obscured the underlying defects causing wafer and cell breakage, and has contributed to the underdevelopment of PV technology pathways with cost reduction potential. For example, thinner wafers represent a promising path toward reduced materials costs and higher efficiency,[18] yet these benefits have been offset by lower production yields due to higher breakage. Thus, there is a need to image and quantify inhomogeneously distributed stresses in crystalline silicon material, in order to quantify the influence of local defects on strength.

In this contribution, we demonstrate the potential of infrared birefringence imaging (IBI) to characterize the spatial distributions of internal stresses in mc-Si solar cell wafers on the micron scale. We begin by demonstrating a method to decouple bulk microdefect-related stresses and thermally induced residual stress. Then, we isolate and decouple the unique birefringence signals generated by common bulk microdefects [including dislocations, silicon carbide inclusions, silicon nitride inclusions, grain boundaries (GBs), and twin bands], elucidating the microscopic origins of the observed birefringence signals. Lastly, we correlate internal stresses observed using IBI with data obtained by other common structural and electrical characterization techniques, highlighting the fact that mc-Si bulk microdefects have profound and interrelated mechanical and electrical effects on solar cells.

II. MATERIALS AND METHODS

A. Materials

We investigated stress distributions in three mc-Si materials: directionally-solidified ingot mc-Si,[19] string ribbon

a)Electronic mail: buonassisi@mit.edu.

silicon,[20,21] and dendritic web.[22] The first two materials are in commercial production, with ingot mc-Si accounting for approximately half of all cells currently produced. Dendritic web is not produced commercially today, but was included in this study as a "model structure" (single crystalline with one twin boundary, with well defined grain orientation and defect distribution[23]).

Ingot mc-Si slabs 1 mm thick were sliced vertically from near an ingot top and polished on both sides. String Ribbon (180–220 μm thick) and Dendritic Web (70–113 μm thick) samples were measured as-grown; their surfaces are typically microscopically smooth directly from growth.

B. IBI

1. Background: Birefringence and its measurement

Birefringent materials induce a phase difference in perpendicular components of light due to a difference in the principal refractive indices (n_1 and n_2); this phase difference can be expressed as a "retardation" value ($\Delta\lambda$), in units of length. In photoelastic materials, such as silicon, the difference in indices can arise due to stress.[24] We denote the direction of light propagation through the thickness of the sample as z. The retardation, assuming a constant stress state along z, is related to stress through the following equation:

$$\frac{\Delta\lambda}{d} = (n_1 - n_2) = C \cdot (\sigma_1 - \sigma_2) = C \cdot 2\tau_{\mathrm{max}}, \quad (1)$$

where d is the thickness along z, C is the material-dependent stress-optic coefficient, σ_1 and σ_2 are the principal stresses in the plane perpendicular to z, and τ_{max} the corresponding maximum shear stress.

The linear relationship between the difference in principal refractive indices and stresses in Eq. (1) is valid for optically isotropic materials, in which the stress-optic coefficient, C, is constant regardless of principal stress direction. In Appendix A, we describe the effects of optical anisotropy on IBI measurements; for the purposes of this manuscript, we assume $C = 1.8 \times 10^{-11}\ \mathrm{Pa}^{-1}$.

2. History of birefringence

Transmission visible and IBI has been widely applied to study bulk defects in transparent cubic crystalline solids,[25,26] including dislocations in sodium chloride,[27–29] silver chloride,[30,31] magnesium oxide,[32] gallium phosphide,[33] cadmium telluride,[34] gallium arsenide,[35] barium nitrate,[36,37] gadolinium gallium garnet,[37,38] and silicon,[39] typically using a microscope with a cross polarizer. In the early 1980s, attempts were made to study residual stresses in mc-Si using point-by-point infrared birefringence mapping, but these were abandoned due to large grain-to-grain variations in signal intensity,[40] believed to be caused by anisotropic polarized reflections or intrinsic anisotropic birefringence.[41,42]

In the mid-2000s, new attempts were made to use IR birefringence mapping[43,44] and imaging[45,46] to measure bulk residual stresses in mc-Si wafers, building on earlier successes with single-crystalline wafers.[47,48] It was proposed that the large grain-to-grain variations in birefringence intensities observed previously may be due to the presence of a variety of microdefects suspected or confirmed to exhibit a birefringence signal, including dislocations[44,49] and GBs.[43,50,51] These initial investigations invite a comprehensive, systematic, and statistically meaningful study to decouple different stress contributions, validated by microstructural measurements.

3. IBI apparatus

In our experiments, IBI was performed using a gray-field polariscope (GFP) constructed by Stress Photonics Inc., described in Ref. 47. A narrow (1101.5 ± 11.5 nm nominal) band pass optical filter was placed above the light source to achieve monochromatic light and a broad-response InGaAs camera (320×256 pixel array) was used for imaging. The camera distance from the sample was varied to obtain both full-wafer and detailed images; a 5× objective was utilized for higher-resolution images. The spatial resolution of the technique is limited by the camera optics and pixel array, and is approximately 100 μm/pixel for full view and 5.7 μm/pixel using the 5× microscope objective. A transmission infrared (TIR) image of the sample was achieved simultaneously, by averaging over an entire rotation of the polarizing filter.

The GFP is able to measure both the magnitude of the principal indices difference ($n_1 - n_2$) and the direction of the first principal refractive index (θ). The quantity ($n_1 - n_2$) is measured by exposing a sample to monochromatic circularly-polarized light, the mathematical equivalent of two perpendicularly-polarized plane waves offset by a quarter wavelength ($\lambda/4$). After the two perpendicularly-polarized plane waves transit through a birefringent sample along different principal refractive indices, they will emerge with a phase offset ($\lambda/4 + \Delta\lambda$). A rotating linear polarizer can measure the ellipticity of the transmitted light, quantifying $\Delta\lambda$.[47] In the transmission mode described, the monochromatic wavelength of light is chosen such that the sample is transparent. For silicon, infrared light is used.

For the GFP, the linear relationship between stress and retardation [Eq. (1)] persists while $\Delta\lambda < \lambda/4$. Linearity holds for shear stresses up to ~100 MPa distributed throughout the wafer thickness, given standard mc-Si measurement conditions (1100 nm light) and samples ($d = 180\ \mu$m). Higher stresses can be measured if sample thickness is reduced, longer wavelength light is used, or the stress is confined to a fraction of the sample thickness. Higher stress values can also be quantified by using a fringe counting technique.[52]

Under the assumption of a constant plane stress state along z, the quantities measured by the GFP are directly proportional to the components of stress typically associated with Mohr's circle ([$\sigma_1 - \sigma_2 = 2\tau_{\mathrm{max}}$], [$2\tau_{\mathrm{xy}}$], and [$\sigma_{\mathrm{x}} - \sigma_{\mathrm{y}}$]), with a proportionality constant of $C \cdot d$ [from Eq. (1)], as illustrated in Fig. 1(b) and described in Ref. 47. Appendix B describes artifacts that can affect quantitative stress measurements, and the steps taken in this study to increase measurement accuracy.

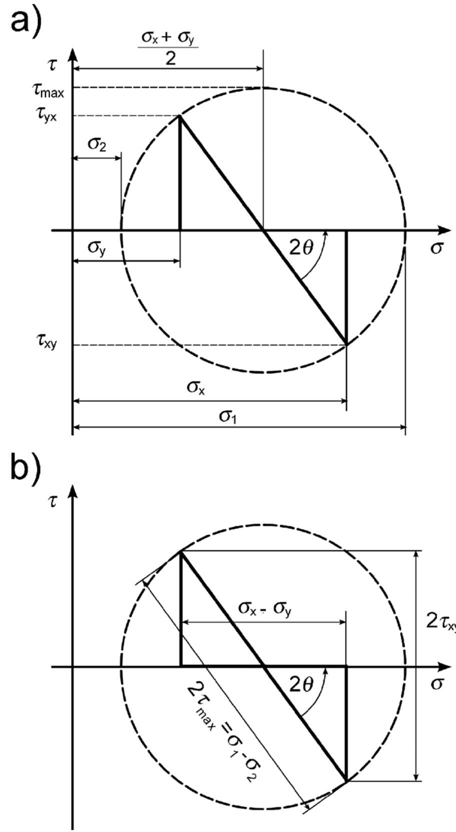

FIG. 1. (a) Mohr's circle and (b) the quantities $(\sigma_1 - \sigma_2)$, $(2\tau_{xy})$, and $(\sigma_x - \sigma_y)$. The quantities in (b) can be measured by a single IBI measurement, whereas quantities in (a) can be determined by comparing IBI measurements before and after stress relief (Fig. 2).

C. Other characterization techniques

Data from IBI measurements were correlated with other measurements from electrical, structural, and chemical characterization techniques.

Minority carrier lifetime measurements were performed using a SemiLab WT2000 microwave photoconductive decay (μ-PCD) tool at the University of Konstanz. Sample cleaning was performed by a piranha (IMEC) clean based on H_2SO_4/H_2O_2 at 80 °C for 20 min followed by an HF (5%) dip for 2 min and rinsing in de-ionized (DI) water. Samples were measured while surface-passivated with an iodine ethanol solution described in Ref. 53.

To determine GB character and grain orientation, electron backscatter diffraction (EBSD, Ref. 54) was performed using a Zeiss Neon 1540 EsB at the University of Konstanz. For GB categorization, the maximum permissible angular deviation was set according to the Brandon criterion [$\Delta\theta \leq 15°\Sigma^{-1/2}$ (Ref. 55)].

Dislocations were revealed with chemical etching at the Massachusetts Institute of Technology. Samples were precleaned in 9:0:1 (referring to the ratio of nitric:acetic:hydrofluoric acids) for 30 s to remove surface contamination, etched in 2:15:36 (known as the Sopori etch[56]) for 30 s to reveal dislocation etch pits, then quenched in 9:0:1 for less than two seconds to prevent staining. Samples were then rinsed with DI water. Dislocation etch pit maps were obtained by imaging the samples using a CanoScan LiDE 700F flatbed scanner. To ensure linearity of this method, a comparison was performed between the grayscale intensity of the scanned image and counts from optical micrographs; linearity was observed in the range of $\sim 10^4$ to $\sim 10^6$ dislocations/cm^2. The principal advantage of using a flatbed scanner is the ability to quickly measure several square decimeters of sample area with a spatial resolution as small as ~3 μm (at 9600 dpi).

Impurity mapping was performed using synchrotron-based x-ray fluorescence microscopy (μ-XRF) at Beamline 2-ID-D (Refs. 57 and 58) of the Advanced Photon Source at Argonne National Laboratory and Beamline 10.3.2 (Ref. 59) of the Advanced Light Source (ALS) at Lawrence Berkeley National Laboratory. These beamlines at third-generation synchrotrons are capable of detecting submicron-sized metal-rich precipitates and inclusions in mc-Si.[60,61] ALS Beamline 10.3.2 was used for large-area maps with a spot size of approximately 16×7 μm^2. High-resolution maps were obtained at APS Beamline 2-ID-D with a beam diameter of 200 nm.

III. DECOUPLING RESIDUAL STRESS AND MICRODEFECT STRESSES

Each pixel of an infrared birefringence image captures the two-dimensional projection of the sum of all stresses within a given sample volume. The observed stresses can be of different origins, including thermally induced residual stress and microdefect-related stresses. For accurate IBI measurement interpretation, it is desirable to distinguish between these two types of stress.

We posit that thermally induced residual stress and microdefect-related stress can be decoupled due to differences in their characteristic length scales: residual thermal stresses vary gradually across the length of a sample, whereas the stress of a microdefect is localized to within a few microns to millimeters around the defect. The creation of a free surface, e.g., by cleaving, relieves both microdefect-related and residual thermal stresses normal to the surface. However, due to differences in characteristic length scale, we expect microdefect-related stresses to only be affected up to a millimeter away from a free edge, whereas the residual thermal stress field should experience a perturbation with a characteristic length on the order of the size of the newly created free surface.

To validate this hypothesis, we compared IBI measurements before and after cleaving a sample of dendritic web silicon—a model material that includes both dislocations and residual stress. In an IBI measurement of a section of the ribbon before cleaving [Fig. 2(a)], we observe a crosshatched stress pattern that closely resembles the pattern of dislocation bands [Fig. 2(b)]. After cleaving the ribbon perpendicular to the growth direction, we observe a faint change in the IBI stress pattern near the incision [Fig. 2(c)]. A subtraction of IBI measurements performed before [Fig. 2(a)] and after [Fig. 2(c)] cleaving is shown in Figs. 2(d)–2(f). These difference images illustrate stresses that vary over the length scale of the cleaved edge, and do not exhibit a crosshatched pattern. We thus conclude that Figs. 2(d)–2(f) illustrate ther-

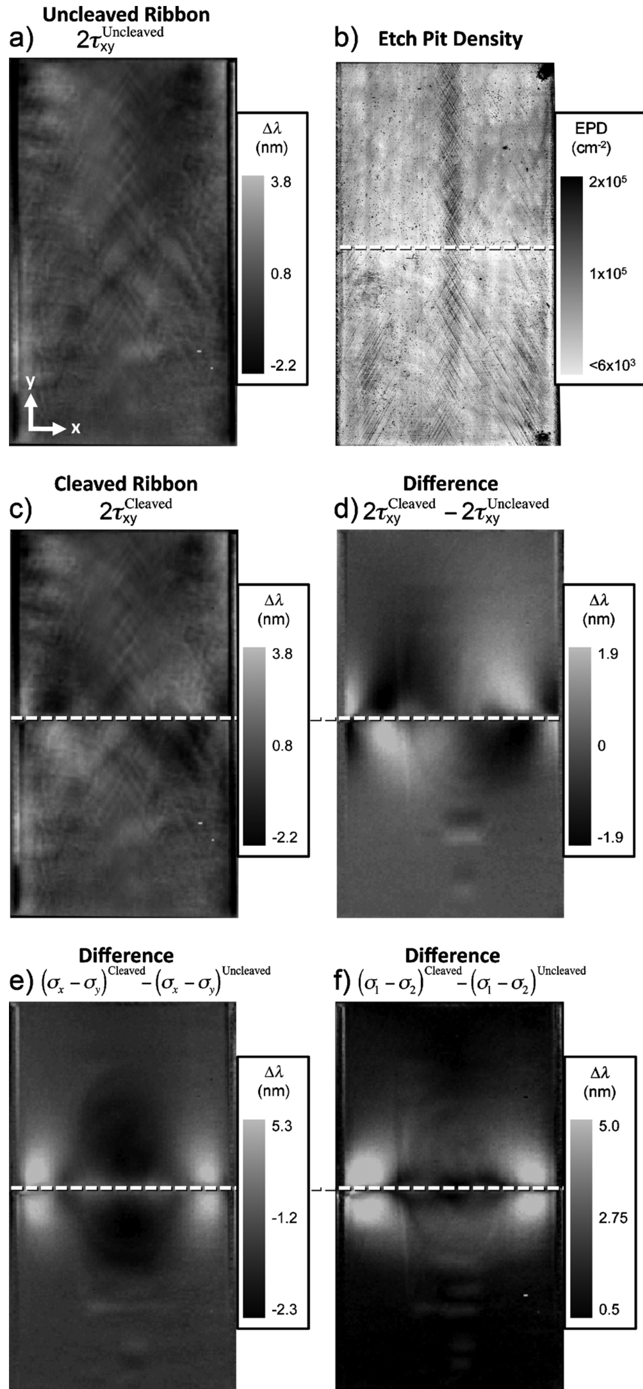

FIG. 2. IBI ($2\tau_{xy}$) measurements of a 4.4×7.5 cm^2 single-crystalline silicon ribbon wafer before cleaving (a) and after cleaving along the dashed line (c) demonstrate the characteristic crosshatch pattern attributed to dislocations, as confirmed by the etch pit density map (b). This crosshatch pattern is not evident in the difference images [(d)–(f)], which illustrate the residual stress relieved by cleaving. Coordinate system shown in (a).

mally induced residual stress in the y-direction relieved by cleaving. By applying Eq. (1), we determined the stress relief to be on the order of 4 MPa. Equivalent or lower stress values are usually observed for other commercial mc-Si materials; in these cases, one can cleave a wafer by diamond scribing or laser cutting.

The residual stress patterns we observe in Figs. 2(d)–2(f) have been predicted by modeling[62,63] and result from temperature gradients across the ribbon during growth. Similar thermal residual stress patterns have been observed by stress measurements before and after thermal annealing,[63] indicating that other methods of residual stress relaxation besides cleaving are possible (although high-temperature annealing can also change the distribution[64] and the density[65–67] of bulk microdefects).

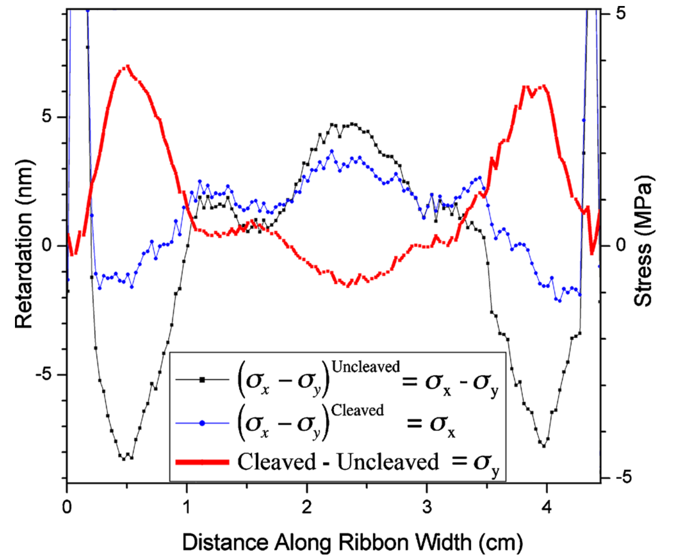

FIG. 3. (Color online) Normal absolute stress (σ_y) evaluation of the ribbon sample shown in Fig. 2, by comparing IBI measurements before and after cleaving.

As an aside, note that a single IBI measurement quantifies shear stress, but not hydrostatic stress [see Fig. 1(b)]. Hydrostatic stress can be measured by comparing IBI before and after cleaving. IBI measurements before cleaving determine the difference between normal stresses, i.e., $(\sigma_x-\sigma_y)$. Cleaving a sample requires that the stress normal to the free surface relaxes, e.g., $\sigma_y|_{cleaved}=0$. By taking the difference of IBI measurements "before" and "after" cleaving, one can cancel the σ_x contribution, and determine σ_y. By analyzing the measurements of Fig. 2 in this manner, one can determine that, as predicted by modeling, the edges of the ribbon were in tension in the y-direction, and the middle of the ribbon in compression in the y-direction, as shown in Fig. 3.

Thus, we conclude that one can distinguish between thermally induced residual stress and bulk microdefect-related stresses due to differences in their characteristic length scales. Additionally, by performing IBI measurements before and after cleaving, one can quantify both hydrostatic and shear components of thermally induced residual stress.

Thermally-induced residual stresses on the order of 5 MPa or less are significantly lower than previous literature reports on full wafers,[51] which do not decouple defect-related stresses from thermally-induced residual stress. As described in Sec. IV, full-wafer measurements are often dominated by defect-related stresses.

IV. TAXONOMY OF MICRODEFECT STRESSES

In crystalline cubic solids, perturbations to the crystalline lattice caused by structural defects or second-phase particles are known to induce characteristic birefringence signals on micron or sub-micron length scales.[27–33,36–38,68] With

IBI, these microdefect-related stresses can be distinguished from macroscopic residual thermal stresses by their smaller length scales and their limited response to cleaving.

Given the plethora of microdefect types in mc-Si, we systematically isolate and measure the most common types with IBI, elucidating their stress "fingerprints." In some cases, we employ finite element analysis (FEA) in conjunction with microstructural information to identify the origin of the stress.

A. SiC and Si_3N_4 Microdefects

Under certain mc-Si ingot growth conditions with supersaturated carbon in the melt, β-SiC particles up to a few hundred microns in diameter can be present in the upper and lower regions of the ingot.[69–72] A similar phenomenon is observed in melts supersaturated with nitrogen, with resulting hexagonal rods of β-Si_3N_4 up to a few tens of microns in diameter and a few millimeters in length.[69–71] Melts supersaturated with both carbon and nitrogen can produce mc-Si material with the presence of both microdefect types.[69–71]

Using infrared transmission microscopy with a 5× objective, we detected several β-SiC particles in a 1 mm thick vertical slice extracted from the upper region of an mc-Si ingot. Infrared microscope and IBI measurements of a β-SiC/β-Si_3N_4 microdefect cluster are shown in Fig. 4. A false-color diagram [Fig. 4(b)] is provided to distinguish β-SiC and β-Si_3N_4 microdefects, based on the authors' experience of a previous investigation.[70]

IBI measurements [Fig. 4(c)] indicate a radially decaying stress surrounding each β-SiC particle. The stress direction [Fig. 4(d)] indicates that the first principal stress component σ_1 is oriented normal to the β-SiC/Si interface. In comparison, very little stress is evident in the immediate vicinity of β-Si_3N_4 rods.

These observations can be explained by considering the origins and material properties of the embedded particles. Because of the complex structure[69] of β-SiC microdefects, their presence in "rashes,"[70] and kinetic limitations for carbon point defect transport in solid silicon,[73] it is believed that these particles form in the melt and are incorporated into the solid ingot at instabilities in the advancing solidification front.[69,73,74] As the ingot cools from 1414 °C to room temperature, the mismatch between the coefficients of thermal expansion (CTE) of the β-SiC, β-Si_3N_4, and silicon matrix results in stress surrounding these microdefects.

The relationship between interfacial stress and observed birefringence can be understood as follows: for a spherical β-SiC inclusion in an infinite Si matrix, the stress magnitude at the Si interface is independent of particle size, depending only on the CTE mismatch and elastic moduli. The radial

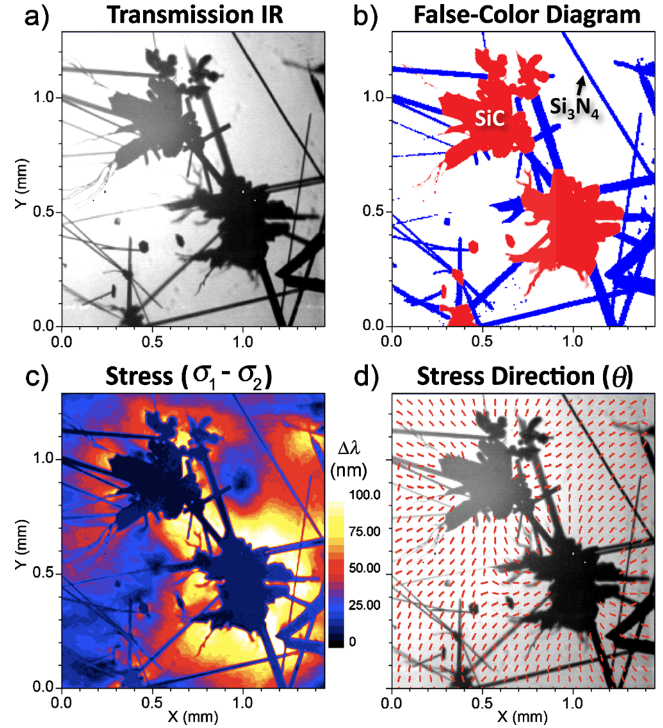

FIG. 4. (Color online) Silicon carbide and nitride inclusions in ingot mc-Si. Large tensile stresses, which decay in the radial direction, are observed surrounding the β-SiC inclusions.

extent of the stress field is observed to be on the order of the particle size. Since the birefringence measured by IBI at an inclusion is a projection of a three-dimensional (3D) stress field, as illustrated in Fig. 5(a), the birefringence is expected to vary linearly with particle size, when the sample thickness is much larger than the particle diameter.

The observed retardation is related to stress by rephrasing Eq. (1) as an integral over the thickness of the sample

$$\Delta\lambda = C\int_0^d 2\tau_{\max}(z)dz, \tag{2}$$

where d is the sample thickness, illustrated in Fig. 5(a). Via Eq. (2), it is understood that larger inclusions should generate a larger birefringence signal, as seen in our experiments. Additionally, inclusions close to a free surface are expected to have smaller birefringence. For example, in Fig. 4(c), the two β-SiC particles are of comparable size, though the upper particle has a surrounding birefringence signal of smaller magnitude. An optical microscope image shows that this particle is near the surface of the sample, so the retardation integral of Eq. (2) is approximately halved. As the β-Si_3N_4 rods have sizes an order of magnitude smaller than the β-SiC

TABLE I. Sets of material parameters used to simulate radial birefringence linescans shown in Fig. 5(c). From Refs. 43, 78, and 79.

	Set 1	Set 2	Set 3
Stress-optic coefficient (Pa^{-1})	1.8×10^{-11}	1.4×10^{-11}	1.4×10^{-11}
Temperature above which stress relief occurs (°C)	550	550	300
β-SiC Young's modulus (E)	370 GPa	314 GPa	370 GPa

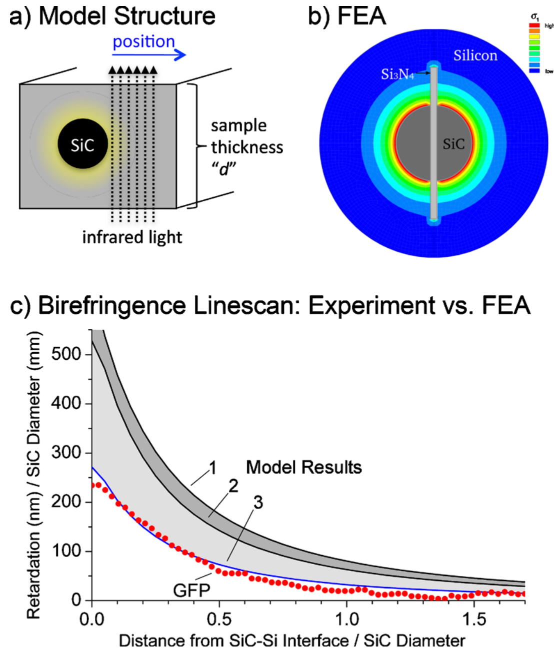

FIG. 5. (Color online) FEA of a model structure (a) predicts the stress field surrounding a β-SiC sphere and a β-Si_3N_4 rod due to CTE mismatches (b). Large stresses are predicted at the β-SiC particle, as seen experimentally in Fig. 4(c). The stress magnitude linescans starting at the β-SiC/Si interface (c) compare experimental IBI data (red dots) to FEA simulations using three different sets of material parameters given in Table I.

particles, as well as a smaller stress magnitude at the interface, we expect the birefringence signal due to the β-SiC particles to dominate.

To confirm these deductions, we modeled an inclusion of a β-SiC sphere embedded in silicon [Fig. 5(a)] using the FEA software ANSYS. It is assumed in the model that stress generated by CTE mismatches above the silicon brittle-to-ductile transition temperature (550 °C, Ref. 75) is relieved via plastic deformation. Consequently, the model assumes that all stress observed in room-temperature measurements originates from linear elastic deformation generated below the silicon brittle-to-ductile transition. All materials are assumed to have linear-elastic, isotropic material behavior. Hence, silicon is modeled with isotropic material parameters using the averaging method following Voigt[76] with the anisotropic material parameters from Ref. 77, resulting in Young's modulus (E) of 166 GPa and Poisson ratio (ν) of 0.217. For silicon carbide, ν=0.188 was assumed, and E was varied according to Table I. For silicon nitride, E=300 GPa, ν =0.24 was used.[80] The temperature-dependent CTEs of β-SiC and Si can be found in Refs. 81 and 82, respectively. The CTE of β-Si_3N_4 was assumed constant with respect to temperature, according to Ref. 80. Note that the model is very sensitive to small changes in CTE; if a temperature-invariant CTE is used, stresses can deviate by 2–3×.

The simulated stress pattern [Fig. 5(b)] and direction are in good qualitative agreement with our experimental results [Fig. 4(c)], as well as birefringence images of inclusions in other cubic crystals.[25,68] These are also in good agreement with recent calculations by M'Hamdi and Gouttebroze.[83] Although M'Hamdi and Gouttebroze use different material parameters, the given analytical equations agree with our FEA simulation. Furthermore, their results regarding the effect of plastic deformation above the brittle-ductile transition temperature show that our assumption to neglect the formation of stress above the brittle-ductile temperature is a good approximation.

To test quantitative agreement, radial linescans from the β-SiC/Si interface from IBI measurements of an isolated β-SiC inclusion were compared with the finite element model [Fig. 5(c)]. The retardation values are linearly proportional to particle diameter $2r$ at a distance $k \cdot 2r$ from the β-SiC/Si interface, where k is a constant. Thus, we normalize the x- and y-axes of Fig. 5(c) to $2r$, using the average diameter of the actual β-SiC inclusion to normalize the IBI measurements. Given the variation and anisotropy of β-SiC material properties in the literature,[81,84–87] two sets of material constants were used to probe extreme upper and lower bounds for stress. These two sets of material parameters are provided in Table I, and correspond to curves 1 and 2 in Fig. 5(c).

We analyzed 40 β-SiC particles with this method; our IBI data consistently falls below the lower bound (curve 2). We achieve better agreement between FEA results and our data if we assume stress relief can occur above 300 °C [curve 3 in Fig. 5(c)], or if a different set of CTEs are used. Using these assumptions, the average stress $(\sigma_1 - \sigma_2)$ was determined to be 24 MPa at the β-SiC/Si and 12 MPa β-Si_3N_4/Si interface. Possible mechanisms for stress relaxation below the brittle-to-ductile transition temperature include the formation of β-SiC microcracks and β-SiC/Si interface defects, which were previously observed[88] in high-resolution transmission electron microscope (TEM) measurements.

Our FEA calculations [curve 3 in Fig. 5(c)] indicate tensile normal stress surrounding isolated β-SiC particles, and compressive normal stress surrounding isolated β-Si_3N_4 particles. When β-SiC clusters and β-Si_3N_4 microdefects are in close proximity, the tensile stress state of the larger β-SiC tends to dominate.

B. Dislocations

Dislocations, one-dimensional line defects[89] present in mc-Si ribbons[23,90] and ingots,[91,92] can form to relieve thermal stresses during crystal growth. Previous studies imaged and modeled the birefringence associated with screw,[37] edge,[38] and mixed[28–34] dislocations in other cubic crystalline solids, both as single dislocations and in bands. It has been presumed that dislocations in mc-Si should exhibit a detectable birefringence signature,[44] in agreement with other strain measurement techniques such as micro-Raman spectroscopy[93] and x-ray topography.[23] Low-resolution IBI measurements by Li[49] suggested a strong positive linear correlation between dislocations and birefringence signal intensity in ribbon mc-Si, although subsequent measurements by Garcia[94] suggested a negative square-root dependence.

For this experiment, we analyzed dislocation-rich grains in ingot mc-Si, string ribbon, and dendritic web materials. Regions within large grains were selected to avoid the convolution of other defect types on IBI measurements. Regions

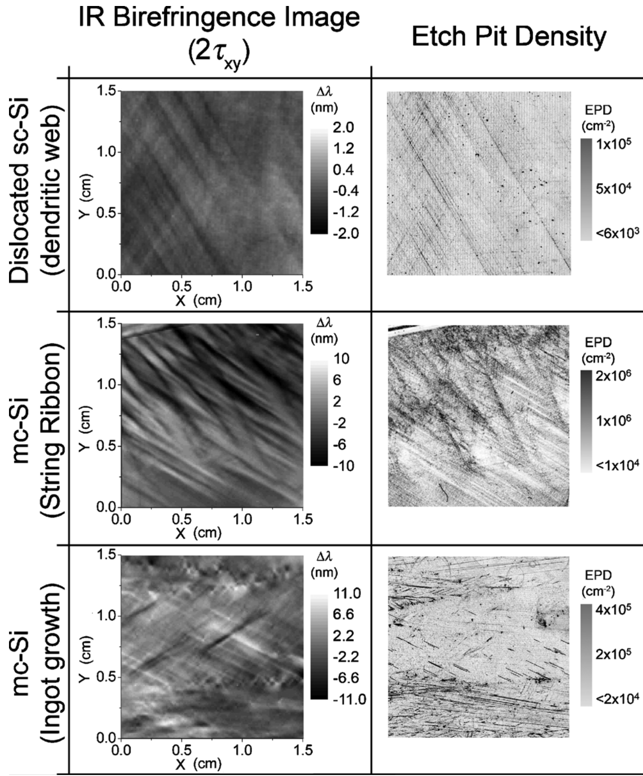

FIG. 6. IBI ($2\tau_{xy}$) and dislocation etch pit density measurements for three different silicon materials: dislocated single-crystalline silicon (dendritic web), and two types of mc-Si (string ribbon and ingot mc-Si). Band-like features in IBI measurements correlate well with dislocation bands.

of interest were imaged with a close-up 1× objective, to cover a statistically meaningful sample area with high resolution. The high resolution imaging nature of IBI combined with a high-sensitivity camera enable a detailed understanding of the relationship between microstructure and birefringence signal at dislocations in mc-Si.

IBI and dislocation density measurements are shown in Fig. 6. The good qualitative agreement between these measurements suggests the band-like intragranular features observed in IBI indeed are associated with bands of dislocations. IBI retardation values associated with mc-Si dislocation bands are typically in the range of 0.1 to 13 nm for wafers ranging between 100 μm and 1 mm thickness.

While qualitatively convincing (Fig. 6), the quantitative relationship between birefringence and dislocation density is observed to vary from grain to grain. It has been shown in other materials that birefringence varies depending on dislocation type and orientation.[26] As mc-Si contains a variety of grain orientations and dislocation types, a quantitative correlation between IBI and dislocation density in mc-Si likely requires *a priori* knowledge of grain texture, and possibly even dislocation type distribution.

IBI measurements on whole ribbon Si samples indicate that the first principal stress direction is typically parallel or perpendicular to the direction of growth, as expected from thermal modeling (Ref. 95). As the direction of maximum shear stress is oriented 45° relative to the principal stresses,[96] it is not surprising that dislocation bands often appear to form diagonal or cross-hatched patterns, along the slip plane

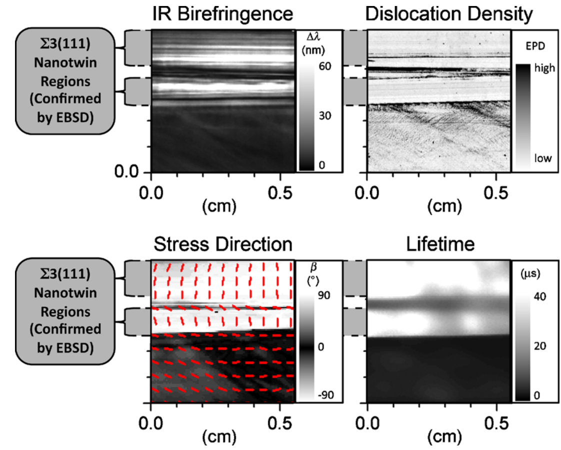

FIG. 7. (Color online) The strong IR birefringence ($\sigma_1 - \sigma_2$) signal in (a) is attributed to nanotwinned regions, as confirmed by (b) dislocation etch pit density and (d) lifetime maps. The direction of the first principal stress in (c) is usually perpendicular to the direction of twin propagation.

most closely aligned to 45° relative to the growth direction.[31,97] Although 3D stress fields within ingots are more complex,[91,92] a similar relationship between principal stress direction and dislocation band formation is expected.

C. Twin bands

Ribbon Si thicker than 100 μm and ingot mc-Si can contain regions several millimeters wide with densely packed twin boundaries separated by as little as a few nanometers.[98–100] These nanotwinned regions, commonly called "twin bands," are associated with high minority carrier lifetimes and low dislocation densities.[100,101]

In our experiment, string ribbon samples were analyzed by IBI with a close-up 1× objective. A nanotwinned band and an adjacent nontwinned grain were identified by EBSD. The IBI of this region shown in Fig. 7 illustrates a very large birefringence signal at the nanotwinned regions, in agreement with previous studies on silicon and other materials.[43,44,50,51]

The microstructural origin of the birefringence caused by these twin bands appears not to be related to isolated dislocations, since one often observes low dislocation densities [Fig. 7(b)] and high minority carrier lifetimes [Fig. 7(d)] in heavily twinned regions of mc-Si, consistent with a wide body of literature.[20,21,100–103] The concentration of metal-rich precipitates at twin boundaries is typically very low, unless pile-up dislocations are present;[104] unlike β-SiC microdefects, there are few nucleation points for metal impurity precipitates due to the highly reconstructed defect core structure.

It is unclear, whether the birefringence observed at twin boundaries originates from the unique crystallography of these regions, or from actual strained crystalline silicon. On one hand, it is worth noting that evidence for strain at nanotwinned regions has been observed by Raman spectroscopy,[93] TEM,[105] and other methods.[51] The stress magnitude and direction observed by IBI are consistent with a model proposed by Werner, Möller, and Scheerschmidt,[99,105,106] whereby carbon atoms within the

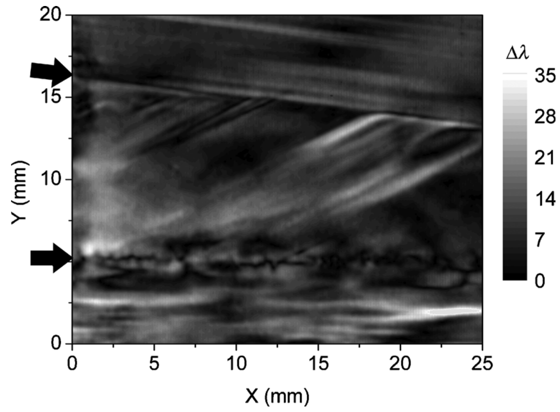

FIG. 8. IBI image ($\sigma_1-\sigma_2$) of nontwinned GBs. Some GBs exhibit periodic localized stresses, while others are largely stress-free. Arrows denote the two GBs in the image above.

twin boundary core structure generate a tensile strain because of the small Si–C bond length. On the other hand, similar birefringence patterns observed at nanotwinned regions in (zincblende) cadmium telluride[34] suggest alternative explanations, possibly intrinsic to the defect microstructure itself. The crystal structure within a twin boundary core deviates significantly from the diamond cubic silicon lattice, thus it is conceivable a change in intrinsic birefringence could occur. Further investigations are needed to explore the physical origin of birefringence at nanotwinned regions.

With very few exceptions, we observe the direction of the first principal stress component perpendicular to the propagation direction of the twin bands [Fig. 7(c)]. Assuming nanotwinned regions to be strained, this result suggests the possibility of tensile strain normal to the twin boundaries. Supporting this hypothesis is the observation that brittle fracture in ribbon and ingot mc-Si samples frequently occurs along twin bands.

D. Nontwinned GBs

Besides twins, ingot mc-Si typically contains several other types of GBs, including various coincident site lattice (CLS) boundaries, small-angle, and large-angle GBs. A birefringence mapping study by Fukuzawa[44] reported generally low retardation values for nontwinned boundaries, varying slightly depending on type.

An IBI measurement with a 1× objective on two GBs in mc-Si is shown in Fig. 8. One GB exhibits a small and uniform birefringence signal, while the other exhibits isolated higher stress concentrations approximately 1.3 mm apart. These GBs were analyzed by μ-XRF at APS Beamline 2-ID-D (sensitive to particles 30 nm in diameter or larger), but no metallic impurities were detected at either GB. Due to scan size limitations (high-resolution μ-XRF scanning areas are limited to approximately 100×10 μm^2 at this beamline), it is plausible that impurity-rich particles exist along the GBs outside the scanned areas.

These initial results warrant a more thorough investigation considering GB character, grain misorientation, faceting, dislocation density, and nonmetallic impurity decoration to elucidate the underlying microstructural causes for the stress variations detected by IBI.

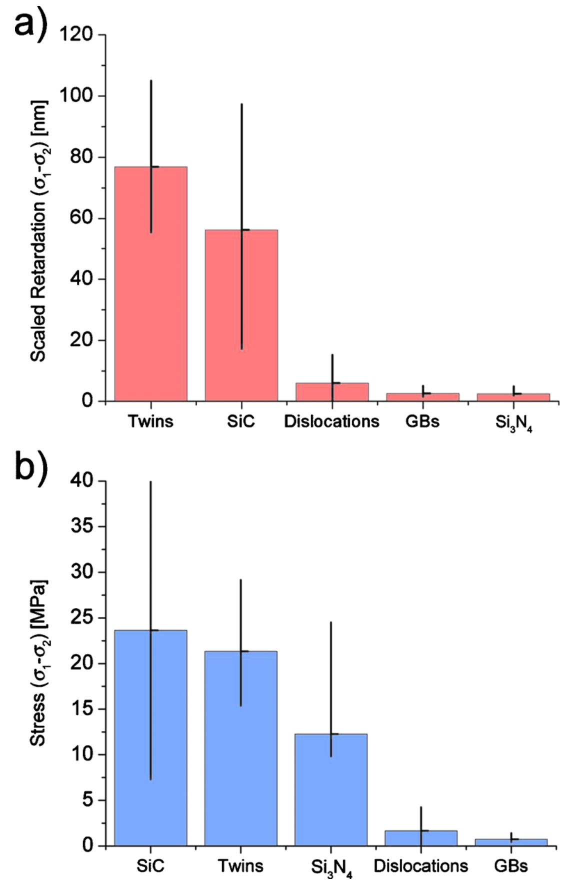

FIG. 9. (Color online) (a) Comparison of IBI-measured retardation values and (b) conversion to stress values ($\sigma 1-\sigma 2$) among defect types.

E. Comparison of individual defect types measured by IBI

The magnitudes of IBI signals for the five defect classes described above are compared in Fig. 9. Retardation values for defects extending through the entire thickness of the wafer (i.e., twins, dislocations, and GBs) are scaled to a wafer thickness of 200 μm. These retardation values are converted to stress in Fig. 9(b) by applying Eq. (1). The stress values for the β-SiC and β-Si_3N_4 microdefects at the silicon/defect interface were found through comparison between FEA and retardation values.

The defect with the strongest IBI signal is the twin band, though the β-SiC microdefect generates the largest stress. Despite its relatively small size, which results in a small IBI signature, the β-Si_3N_4 microdefect is responsible for a large local stress. Much lower IBI signals were observed at dislocation bands and nontwin GBs, although future modeling of these defects may reveal large local stresses over very small length scales.

V. FULL-WAFER IMAGING: DECOUPLING INDIVIDUAL STRESS CONTRIBUTIONS IN IBI MEASUREMENTS

Large-area IBI measurements can be performed on entire wafers or bricks of silicon, and may be useful in industry as

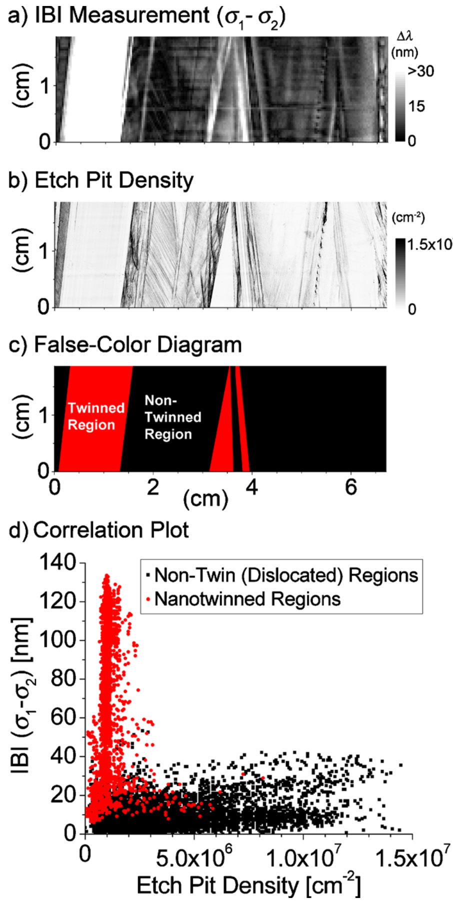

FIG. 10. (Color online) (a) IBI ($2\tau_{xy}$) and (b) dislocation etch pit measurements on a ribbon silicon wafer. Two distinct regions can be observed: higher-stress, dislocation-free nanotwinned regions (such as those featured in Fig. 7) shown in gray (red online) in (c); and lower-stress, nontwinned, dislocated regions (such as that featured in Fig. 6) shown in black in (c). A correlation plot highlights this distinction (d).

a quality-control test. In each region of a large-area IBI measurement, there is typically one dominant defect type, with a unique IBI signature, including signal intensity, first principal stress direction, stress pattern, and length scale, as shown in Sec. IV. To accurately interpret a large-area IBI measurement, it is necessary to utilize these unique signatures to decouple various defect types.

As an example of a large-area IBI measurement, we present an IBI $2\tau_{max}$ image over a full ribbon silicon wafer section in Fig. 10(a). Based on the unique stress signatures of various defect types presented in Sec. IV, we label the dominant defect type in each characteristic region of the sample [Fig. 10(c)]. The strong, rectilinear IBI signature suggestive of twin bands is confirmed by defect etching [Fig. 10(b)]. The fainter, band-like features suggestive of dislocation bands are likewise confirmed by defect etching. The faint horizontal features observable in the IBI measurement [Fig. 10(a)] are caused by local thickness variations. Residual thermal stresses appear to account for a small fraction of the IBI signal.

A second example of a large-area IBI measurement interpretation is shown in Fig. 11. Here, a millimeter-thick vertical slice of mc-Si ingot material is revealed to contain several β-SiC inclusions via unpolarized infrared transmission

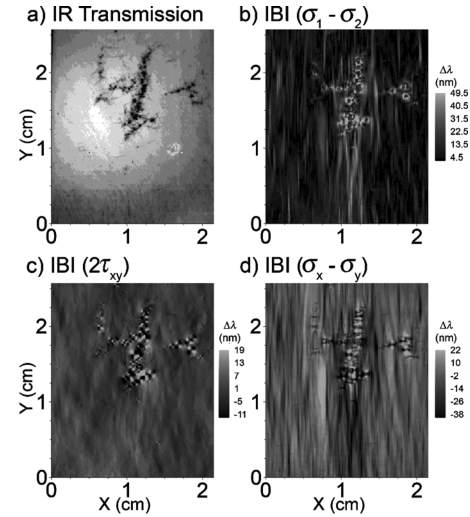

FIG. 11. Millimeter-thick vertical slice of mc-Si ingot material examined with IBI. Unpolarized infrared transmission imaging (a) reveals β-SiC inclusions, while an IBI measurement [(b)–(d)] reveals dislocation bands in addition to β-SiC microdefects.

imaging [Fig. 11(a)]. IBI measurements reveal the stress field surrounding β-SiC inclusions [Fig. 11(c)], as well as dislocation bands [Figs. 11(b) and 11(d)]. As TIR imaging is already employed during mc-Si brick inspection following crystal growth, it is possible that IBI may be employed to determine thermal stress and dislocation density at this stage, with minimal adjustment to process metrology.

VI. EFFECT OF STRESS ON MANUFACTURING YIELD AND EFFICIENCY

A. Effect of stress on manufacturing yield

The largest tensile stresses in mc-Si are associated with β-SiC inclusions and nanotwin bands (Figs. 4, 7, and 9). Residual tensile stress is known to lower the critical crack length and applied load necessary to fracture brittle silicon wafers. This can have catastrophic consequences for mechanical yield during wafer manufacturing and handling. In fact, it is not uncommon to observe a ribbon silicon wafer fracture along the length of a nanotwin band, consistent with the direction of the first principal stress component [Fig. 7(c)]. From purely the perspective of process yield optimization, it is desirable to reduce or eliminate the concentrations of these defects, as suggested by Chen.[50]

Improving crystal growth has consistently been demonstrated to be the most promising path to suppress defect formation. One may successfully suppress tensile defect formation by growing in a low-carbon environment (to suppress β-SiC) and avoiding large thermal stresses, especially at temperatures a few hundred degrees Celsius below melting (to suppress nanotwin bands). For ribbon growth, thinner ribbons may also suppress nanotwin band formation, as suggested by Wallace.[98]

B. Direct effects of stress on minority carrier lifetime

Solar cell efficiency is a strong function of minority carrier lifetime.[107–109] Under one-sun injection conditions, life-

time in mc-Si solar cells is limited primarily by microdefect recombination activity, which is governed by defect capture cross section and energy level(s) within the bandgap.[110,111] Since these parameters are typically only weakly influenced by stresses in the tens of megapascals range,[112,113] the direct effect of low stress levels on minority carrier lifetime is minimal.

To illustrate this point, consider that nanotwinned regions in Fig. 7 exhibit a strong IBI signal, but these defects have low intrinsic recombination activity.[100,101] Hence, nanotwinned regions exhibit high minority carrier lifetimes despite being highly stressed, reaffirming similar conclusions reached by Chen.[50] In contrast, the neighboring dislocation-rich grain in Fig. 7 has a much lower lifetime and birefringence signal, due to the high recombination activity of dislocations in silicon.[110,114]

C. Indirect effects of stress on minority carrier lifetime

Stress can have a large indirect effect on minority carrier lifetime in mc-Si, by regulating the formation and kinetics of lifetime-limiting defects such as dislocations and impurities. For example, dislocations can be formed via stress relaxation above the brittle-to-ductile transition temperature, reducing minority carrier lifetime.[115–117] Thermal gradients during crystal growth[23,90–92] or cell processing[66,67] are well known to provoke dislocation formation, but similar pathways involving microdefect-related stresses have generally been underappreciated. We observe local stress along GBs (Fig. 8); recent FEA simulations by Usami[118] suggest that GB stresses can play a critical role in generating intragranular dislocations. Likewise, large stresses have been observed in the vicinities of β-SiC inclusions (Fig. 3), from which dislocation clusters have been observed to originate.[100,119] By examining our results in the context of a growing body of literature, we conclude that stressed microdefects can indirectly impact minority carrier lifetime by generating dislocations.

Stress is known to alter the distribution of deleterious metallic impurities in mc-Si. Copper, nickel, and iron silicide precipitates are frequently observed aggregated at stressed β-SiC inclusions, as shown in the μ-XRF measurements in Fig. 12 and confirmed by literature reports.[120,121] Considerably fewer metal silicide precipitates are observed at β-Si_3N_4 inclusions,[120] which are associated with lower stresses [Fig. 3(c)].

While stress facilitates impurity precipitation, it is not a sufficient condition. Nanotwinned regions also appear to be highly stressed, yet they exhibit low impurity precipitate decoration,[104] likely due to the scarcity of suitable heterogeneous nucleation sites in the defect core structure.

VII. CONCLUSIONS

IBI is presented as a powerful tool to measure stresses and identify bulk microdefects in mc-Si. We are able to distinguish between thermally induced residual stress and bulk microdefect-related stresses due to differences in their characteristic length scales. Both normal and shear components

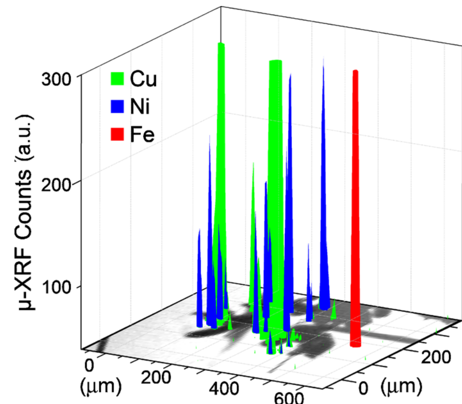

FIG. 12. (Color online) The dark features in the X-Y plane represent a β-SiC microdefect [IR transmission image, from Fig. 4(a)]. The colored spikes represent metal clusters detected by μ-XRF. These metal clusters are visibly located at or near the β-SiC microdefect, within the region of highest stress evidenced in Fig. 4(c).

of thermally induced residual stress can be quantified by performing IBI measurements before and after creation of free surfaces, where stresses are relieved.

Through comparison of IBI measurements with defect characterization and FEA, we decoupled and described the unique IR birefringence patterns, magnitudes, and origins of common microdefects in mc-Si solar cell materials, including β-SiC and β-Si_3N_4 microdefects, twin bands, nontwin GBs, and dislocation bands. FEA suggests the observed radial tensile stress surrounding β-SiC microdefects arises from a CTE mismatch between the inclusion and the surrounding silicon matrix; this observation can help explain impurity gettering to the β-SiC/Si interface, suggests the prospect for lower wafer mechanical yield when β-SiC inclusions are present, and explains why such defects serve as efficient nucleation points for dislocations. Twin bands also exhibit a strong IR birefringence; suspected tensile stresses oriented perpendicular to the direction of propagation of the twins also suggest the prospect of lower wafer mechanical yield; this is consistent with observation of wafer fracture along twins. By comparison, dislocation bands exhibit a weak birefringence signal, yet are distinguishable by their band-like structure and frequent characteristic alignment along slip planes approximately 45° relative to the direction of maximum axial stress during crystal growth.

Distinguishing between these different defect types is essential to understanding the complex correlations between minority carrier lifetime maps and stress images. While some defect types are associated with high lifetimes (e.g., twin bands), others are known to lower lifetime (e.g., dislocations). A direct correlation between lifetime and small stress levels detected by IBI is inconsistent, because small stresses do not appreciably alter defect energy levels or capture cross sections. However, both thermal and microdefect-related stresses can have a large indirect influence on lifetime, e.g., by generating locally high concentrations of dislocations via plastic deformation.

If properly developed, we believe IBI may eventually enable predictive yield and efficiency analysis. With stronger light sources and larger fields of view, it may be possible to

perform (tomographic) IBI to detect microscopic defects in entire ingots or bricks of mc-Si, or on mc-Si modules, ensuring enhanced quality control with minimal additional cost in a nondestructive and contactless manner.

ACKNOWLEDGMENTS

We acknowledge A. S. Argon, A. E. Hosoi, G. H. McKinley, and G. Barbastathis for insightful comments, J. Lesniak for GFP equipment support, A. Zuschlag for EBSD support, S. Olibet for lifetime measurement support, H.-J. Axman for providing String Ribbon samples, and D. P. Fenning, S. Hudelson, B. Pope, A. Fecych, B. K. Newman, and M. I. Bertoni for μ-XRF and laboratory support. Financial support for this research was provided by the U.S. Department of Energy, under Contract No. DE-FG36-09GO19001, and through the generous support of Doug Spreng and the Chesonis Family Foundation. Individual researcher support was provided by the Paul E. Gray (1954) Endowed Fund for UROP and MISTI-Germany (V. Ganapati), the Federal Ministry of Education and Research (BMBF) within the project "SiThinSolar" (Contract No. 03IP607) (S. Schoenfelder, R. Koepge), the German Federal Law on Support in Education, BAfoeG (S. Oener). The Advanced Light Source and the Advanced Photon Source are supported by the Director, Office of Science, Office of Basic Energy Sciences, of the U.S. Department of Energy under Contract Nos. DE-AC02-05CH11231 and DE-AC02-06CH11357, respectively.

APPENDIX A: SILICON STRESS-OPTIC COEFFICIENT

Equation (1) assumes an isotropic material, i.e., C is invariant with crystal orientation. However, the stress-optic coefficient of silicon is known to vary with respect to crystallographic orientation. In this appendix, we (a) describe and quantify the effect of anisotropic stress-optic coefficient values for silicon, and (b) summarize the range of experimental stress-optic coefficient values reported in literature. With this information, one can estimate the error of converting retardation to stress $(\sigma_1-\sigma_2)$.

The stress-optic coefficients for principal stresses as a function of crystal direction can be calculated from the piezo-optical coefficients (π) of a material, according to

$$C_{(001)}(\theta) = \frac{n_0^3}{2}\frac{1}{\sqrt{\frac{\sin^2 2\theta}{\pi_{44}^2}+\frac{\cos^2 2\theta}{(\pi_{11}-\pi_{12})^2}}} \tag{A1}$$

from Ref. 78. The maximum value occurs along the (100) orientation (θ=0), while the minimum occurs along the (110) orientation (θ=45°). As described in Ref. 52, a small angle may be present between (n_1-n_2) and $(\sigma_1-\sigma_2)$; this angle is approximately ±10°, depending on crystal orientation. Herein, we ignore the small angle offset and approximate Eq. (1) to be valid.

Anisotropic effects aside, there is a range of values for π and C reported in the literature.[52,78,122,123] Table II summarizes the literature range of piezo-optical coefficients and provides the corresponding stress-optic coefficients when the principal stresses lie in the ⟨100⟩ and ⟨110⟩ directions.

TABLE II. Summary of piezo-optical coefficients from literature, and corresponding stress-optic coefficients calculated from Eq. (A1) for different crystal orientations. For light with 1100 nm wavelength, n_o=3.5 (from Ref. 124).

Reference	$\pi_{11}-\pi_{12}$ ($\times10^{-13}$ Pa^{-1})	π_{44} ($\times10^{-13}$ Pa^{-1})	$C_{\langle100\rangle}$ ($\times10^{-11}$ Pa^{-1})	$C_{\langle110\rangle}$ ($\times10^{-11}$ Pa^{-1})
121	14.4	10.0	3.09	2.14
122	8.48	4.58	1.82	0.98
52	12.22	6.50	2.62	1.39
120	9.88	6.50	2.12	1.39

For our study, we chose a median value for C=1.8 $\times10^{-11}$ Pa^{-1}, unless noted otherwise. We note that this value may vary by as much as a factor of two, given the uncertainties described above.

APPENDIX B: IDENTIFICATION OF EXPERIMENTAL ARTIFACTS

Since IBI captures the relative difference between major and minor polarization directions for each pixel, constant pixel-to-pixel intensity variations should not affect measurement results (assuming detector response is linear with light intensity). Artifacts in IBI measurements can be caused by dichroic effects, anisotropic reflectance, and path length differences caused by spatial noncoherence of the light. The first two effects are intrinsic, wavelength-dependent material properties; measuring IBI at two or more wavelengths of incoming light may help confirm that measurements outputs are consistent. The latter two artifacts are exacerbated by improperly aligned IBI measurement setups; the spatial coherence of the incoming light is essential to reducing anisotropic reflectance and ensuring similar optical path lengths through the sample thickness for each X-Y position in an IBI image [lest the variable d in Eqs. (1) and (2) vary from one pixel to another]. In our study, we minimized the effects of these artifacts by careful system alignment, and, when possible, flat and polished wafers.

To quantify the maximum retardation error, we measured all samples in two orientations (0° and 90°), and determined that the error from measurement to measurement was less than 5 nm absolute for a 180 μm thick sample. For adjacent regions within the same grain, experimental error of retardation was less than 0.2 nm for a 180 μm thick sample.

While elimination of these artifacts is essential for quantitative stress imaging, meaningful qualitative comparisons of IBI measurements are possible. Hence, IBI is fairly robust in diagnosing the locations and identities of bulk microdefects in a nondestructive manner.

[1]T. Surek, *Third World Conference on Photovoltaic Energy Conversion* (IEEE, Osaka, Japan, 2003), Vol. 3, p. 2507.
[2]T. Trupke, R. A. Bardos, M. C. Schubert, and W. Warta, Appl. Phys. Lett. **89**, 044107 (2006).
[3]T. Trupke, R. A. Bardos, M. D. Abbott, P. Würfel, E. Pink, Y. Augarten, F. W. Chen, K. Fisher, J. E. Cotter, M. Kasemann, M. Rüdiger, S. Kontermann, M. C. Schubert, M. The, S. W. Glunz, W. Warta, D. Macdonald, J. Tan, A. Cuevas, J. Bauer, R. Gupta, O. Breitenstein, T. Buonassisi, G. Tarnowski, A. Lorenz, H. P. Hartmann, D. H. Neuhaus, and J. M. Fernandez, *22nd European Photovoltaic Solar Energy Conference and Exhibition* (WIP-Munich, Milan, Italy, 2007).

[4] T. Fuyuki, H. Kondo, T. Yamazaki, Y. Takahashi, and Y. Uraoka, Appl. Phys. Lett. **86**, 262108 (2005).
[5] M. Kasemann, W. Kwapil, B. Walter, J. Giesecke, B. Michl, M. The, J.-M. Wagner, J. Bauer, A. Schütt, J. Carstensen, H. Kampwerth, P. Gundel, M. C. Schubert, R. A. Bardos, H. Föll, H. Nagel, P. Würfel, T. Trupke, O. Breitenstein, W. Warta, and S. W. Glunz, *Proceedings of the 23rd European Photovoltaic Solar Energy Conference* (WIP-Munich, Valencia, Spain, 2008).
[6] O. Breitenstein, J. P. Rakotoniaina, and M. H. Al Rifai, Prog. Photovoltaics **11**, 515 (2003).
[7] J. Isenberg and W. Warta, J. Appl. Phys. **95**, 5200 (2004).
[8] M. Kaes, S. Seren, T. Pernau, and G. Hahn, Prog. Photovoltaics **12**, 355 (2004).
[9] H. Nagel, A. G. Aberle, and S. Narayanan, Solid State Phenom. **67–68**, 503 (1999).
[10] J. Isenberg, J. Dicker, and W. Warta, J. Appl. Phys. **94**, 4122 (2003).
[11] M. C. Schubert and W. Warta, Prog. Photovoltaics **15**, 331 (2007).
[12] K. Ramspeck, K. Bothe, J. Schmidt, and R. Brendel, J. Mater. Sci.: Mater. Electron. **19**, 4 (2008).
[13] W. Weibull, ASME J. Appl. Mech. **18**, 293 (1951).
[14] C. Funke, E. Kullig, M. Kuna, and H. J. Möller, Adv. Eng. Mater. **6**, 594 (2004).
[15] S. Schoenfelder, M. Ebert, C. Landesberger, K. Bock, and J. Bagdahn, Microelectron. Reliab. **47**, 168 (2007).
[16] K. Wasmer, A. Bidiville, J. Michler, C. Ballif, M. d. Meer, and P. Nasch, *22nd European Photovoltaic Solar Energy Conference* (WIP-Munich, Milan, Italy, 2007).
[17] P. Rupnowski and B. Sopori, Int. J. Fract. **155**, 67 (2009).
[18] W. P. Mulligan, M. A. Carandang, M. Dawson, D. M. D. Ceuster, C. N. Stone, and R. M. Swanson, *21st European Photovoltaic Solar Energy Conference and Exhibition* (WIP-Munich, Dresden, Germany, 2007).
[19] W. Koch, A. L. Endrös, D. Franke, C. Häßler, J. P. Kalejs, and H. J. Möller, in *Handbook of Photovoltaic Science and Engineering*, edited by A. Luque and S. Hegedus, (John Wiley & Sons Ltd., England, 2003).
[20] J. I. Hanoka, Sol. Energy Mater. Sol. Cells **65**, 231 (2001).
[21] G. Hahn and A. Schönecker, J. Phys.: Condens. Matter **16**, R1615 (2004).
[22] R. G. Seidensticker and R. H. Hopkins, J. Cryst. Growth **50**, 221 (1980).
[23] S. L. Morelhão and S. Mahajan, J. Cryst. Growth **177**, 41 (1997).
[24] S. R. Lederhandler, J. Appl. Phys. **30**, 1631 (1959).
[25] B. K. Tanner and D. J. Fathers, Philos. Mag. **29**, 1081 (1974).
[26] N.-B. Ming and C.-Z. Ge, J. Cryst. Growth **99**, 1309 (1990).
[27] R. W. Davidge and P. L. Pratt, Phys. Status Solidi **6**, 759 (1964).
[28] S. Mendelson, J. Appl. Phys. **33**, 2175 (1962).
[29] A. S. Argon, A. K. Nigam, and G. E. Padawer, Philos. Mag. **25**, 1095 (1972).
[30] J. F. Nye, Proc. R. Soc. London, Ser. A **198**, 190 (1949).
[31] J. F. Nye, Proc. R. Soc. London, Ser. A **200**, 47 (1949).
[32] A. S. Argon and E. Orowan, Philos. Mag. **9**, 1003 (1964).
[33] J. Hilgarth, J. Mater. Sci. **13**, 2697 (1978).
[34] G. Kloess, M. Laasch, R. Schwarz, and K. W. Benz, J. Cryst. Growth **146**, 130 (1995).
[35] P. Dobrilla and J. S. Blakemore, J. Appl. Phys. **60**, 169 (1986).
[36] K. Maiwa, K. Tsukamoto, I. Sunagawa, C.-Z. Ge, and N.-B. Ming, J. Cryst. Growth **98**, 590 (1989).
[37] C.-Z. Ge and H.-W. Wang, J. Appl. Phys. **74**, 139 (1993).
[38] J. W. Matthews and T. S. Plaskett, Phys. Status Solidi A **37**, 499 (1976).
[39] F. Lihl, J. Tomiser, P. Skylicky, and M. Kuster, Z. Angew. Phys. **32**, 287 (1971).
[40] E. Sachs, private communication (2008).
[41] J. Pastrnak and K. Vedam, Phys. Rev. B **3**, 2567 (1971).
[42] T. Chu, M. Yamada, J. Donecker, M. Rossberg, V. Alex, and H. Riemann, Microelectron. Eng. **66**, 327 (2003).
[43] M. C. Brito, J. M. Alves, J. M. Serra, R. M. Gamboa, C. Pinto, and A. M. Vallera, Rev. Sci. Instrum. **76**, 013901 (2005).
[44] M. Fukuzawa and M. Yamada, Mater. Sci. Semicond. Process. **9**, 266 (2006).
[45] F. Li, V. Garcia, and S. Danyluk, *Proceedings of the Fourth World Conference on Photovoltaic Energy Conversion*, (IEEE, Kona, Hawaii, 2006), p. 1245.
[46] T. Buonassisi, S. Reitsma, R. Sweeney, M. D. Pickett, W. Huang, J. Lesniak, and M. L. Spencer, *Proceedings of the 22nd European Photovoltaic Solar Energy Conference* (WIP-Munich, Milan, Italy, 2007).
[47] G. Horn, J. Lesniak, T. Mackin, and B. Boyce, Rev. Sci. Instrum. **76**, 045108 (2005).
[48] M. Yamada, Rev. Sci. Instrum. **64**, 1815 (1993).
[49] F. Li, V. Garcia, S. Danyluk, S. Ostapenko, J. Kalejs, and D. Yates, *Fourth World Conference on Photovoltaic Energy Conversion* (IEEE, Waikoloa, USA, 2006), p. 1429.
[50] J. Chen, B. Chen, T. Sekiguchi, M. Fukuzawa, and M. Yamada, Appl. Phys. Lett. **93**, 112105 (2008).
[51] A. Belyaev, O. Polupan, S. Ostapenko, D. Hess, and J. P. Kalejs, Semicond. Sci. Technol. **21**, 254 (2006).
[52] H. Liang, Y. Pan, S. Zhao, G. Qin, and K. K. Chin, J. Appl. Phys. **71**, 2863 (1992).
[53] T. S. Horányi, T. Pavelka, and P. Tüttö, Appl. Surf. Sci. **63**, 306 (1993).
[54] F. J. Humphreys, J. Mater. Sci. **36**, 3833 (2001).
[55] D. G. Brandon, Acta Metall. **14**, 1479 (1966).
[56] B. L. Sopori, Appl. Opt. **27**, 4676 (1988).
[57] Z. Cai, B. Lai, W. Yun, I. McNulty, A. Khounsary, J. Maser, P. Ilinski, D. Legnini, E. Trakhtenberg, S. Xu, B. Tieman, G. Wiemerslage, and E. Gluskin, AIP Conf. Proc. **521**, 31 (2000).
[58] W. Yun, B. Lai, Z. Cai, J. Maser, D. Legini, E. Gluskin, Z. Chen, A. Krasnoperova, Y. Valdimirsky, F. Cerrina, E. D. Fabrizio, and M. Gentili, Rev. Sci. Instrum. **70**, 2238 (1999).
[59] M. A. Marcus, A. A. MacDowell, R. Celestre, E. Domning, K. Franck, A. Manceau, G. Morrison, T. Miller, H. A. Padmore, and R. E. Sublett, J. Synchrotron Radiat. **11**, 239 (2004).
[60] S. A. McHugo, A. C. Thompson, C. Flink, E. R. Weber, G. Lamble, B. Gunion, A. MacDowell, R. Celestre, H. A. Padmore, and Z. Hussain, J. Cryst. Growth **210**, 395 (2000).
[61] T. Buonassisi, A. A. Istratov, M. A. Marcus, M. Heuer, M. D. Pickett, B. Lai, Z. Cai, S. M. Heald, and E. R. Weber, Solid State Phenom. **108–109**, 577 (2005).
[62] J. C. Lambropoulos, J. W. Hutchinson, R. O. Bell, B. Chalmers, and J. P. Kalejs, J. Cryst. Growth **65**, 324 (1983).
[63] T. Buonassisi, S. Reitsma, R. Sweeney, M. D. Pickett, W. Huang, J. Lesniak, and M. L. Spencer, *22nd European Photovoltaic Solar Energy Conference and Exhibition* (WIP-Munich, Milan, Italy, 2007).
[64] E. S. Meieran and I. A. Blech, J. Appl. Phys. **38**, 3495 (1967).
[65] K. Hartman, M. Bertoni, J. Serdy, and T. Buonassisi, Appl. Phys. Lett. **93**, 122108 (2008).
[66] D. Franke, *Third World Conference on Photovoltaic Energy Conversion* (IEEE, Osaka, Japan, 2003).
[67] D. Macdonald and A. Cuevas, *Proceedings of the 16th European Photovoltaic Solar Energy Conference* (WIP-Munich, Glasgow, UK, 2000), p. 1707.
[68] J. W. Matthews, E. Klokholm, V. Sadagopan, T. S. Plaskett, and E. Mendel, Acta Metall. **21**, 203 (1973).
[69] A. K. Søiland, E. J. Øvrelid, T. A. Engh, O. Lohne, J. K. Tuset, and Ø. Gjerstad, Mater. Sci. Semicond. Process. **7**, 39 (2004).
[70] J.-P. Rakotoniaina, O. Breitenstein, M. Werner, M. H. Al Rifai, T. Buonassisi, M. D. Pickett, M. Ghosh, A. Müller, and L. Q. Nam, *Proceedings of the 20th European Photovoltaic Solar Energy Conference* (WIP-Munich, Barcelona, Spain, 2005).
[71] J. Bauer, O. Breitenstein, and J.-P. Rakotoniaina, Phys. Status Solidi A **204**, 2190 (2007).
[72] G. Du, N. Chen, and P. Rossetto, Sol. Energy Mater. Sol. Cells **92**, 1059 (2008).
[73] C. Reimann, M. Trempa, J. Friedrich, S. Würzner, and H.-J. Möller, *Third International Workshop on Crystalline Silicon Solar Cells* (NTNU/SINTEF, Trondheim, Norway, 2009).
[74] H.-J. Möller, C. Funke, and S. Würzner, *Third International Workshop on Crystalline Silicon Solar Cells* (NTNU/SINTEF, Trondheim, Norway, 2009).
[75] J. Samuels and S. G. Roberts, Proc. R. Soc. London, Ser. A **421**, 1 (1989).
[76] W. Voigt, *Lehrbuch der Kristallphysik* (Teubner Verlag, Leipzig, 1910).
[77] J. J. Hall, Phys. Rev. **161**, 756 (1967).
[78] S. He, T. Zheng, and S. Danyluk, J. Appl. Phys. **96**, 3103 (2004).
[79] R. Hull, *Properties of Crystalline Silicon* (INSPEC, Exeter, UK, 1999).
[80] J. F. Shackelford and W. Alexander, *CRC Materials Science and Engineering Handbook*, 3rd ed. (CRC, Boca Raton, FL, 2001).
[81] Z. Li and R. C. Bradt, J. Mater. Sci. **21**, 4366 (1986).
[82] M. Okaji, Int. J. Thermophys. **9**, 1101 (1988).
[83] M. M'Hamdi and S. Gouttebroze, in *24th European Photovoltaic Solar Energy Conference* (WIP-Munich, Hamburg, Germany, 2009), p. 1265.
[84] S. Adachi, *Handbook on Physical Properties of Semiconductors* (Kluwer Academic, Boston, USA, 2004), Vol. 1.
[85] K. Strössner, M. Cardona, and W. J. Choyke, Solid State Commun. **63**,

113 (1987).
[86]W. A. Bassett, M. S. Weathers, T.-C. Wu, and T. Holmquist, J. Appl. Phys. **74**, 3824 (1993).
[87]M. Yoshida, A. Onodera, M. Ueno, K. Takemura, and O. Shimomura, Phys. Rev. B **48**, 10587 (1993).
[88]A. Lotnyk, J. Bauer, O. Breitenstein, and H. Blumtritt, Sol. Energy Mater. Sol. Cells **92**, 1236 (2008).
[89]D. Hull and D. J. Bacon, *Introduction to Dislocations*, 4th ed. (Butterworth-Heinemann, Oxford, UK, 2001).
[90]J. P. Kalejs, J. Cryst. Growth **230**, 10 (2001).
[91]C. Häßler, G. Stollwerck, W. Koch, W. Krumbe, A. Müller, D. Franke, and T. Rettelbach, Adv. Mater. **13**, 1815 (2001).
[92]J. Cochard, S. Gouttebroze, S. Dumoulin, M. Mhamdi, and Z. L. Zhang, *23rd European Photovoltaic Solar Energy Conference* (WIP-Munich, Valencia, Spain, 2008).
[93]M. Becker and H. Scheel, J. Appl. Phys. **101**, 063531 (2007).
[94]V. Garcia, Thesis, Georgia Institute of Technology, 2008.
[95]H. Behnken, D. Franke, H. Kasjanow, A. Nikanorov, and A. Seidl, *Fourth World Conference on Photovoltaic Energy Conversion* (IEEE, Waikoloa, Hawaii, 2006), p. 1175.
[96]R. C. Hibbeler, *Mechanics of Materials*, 7th ed. (Prentice-Hall, Upper Saddle River, New Jersey, 2008).
[97]A. Argon, *Strengthening Mechanisms in Crystal Plasticity* (Oxford University Press, USA, 2007).
[98]R. L. Wallace, J. I. Hanoka, A. Rohatgi, and G. Crotty, Sol. Energy Mater. Sol. Cells **48**, 179 (1997).
[99]K. Scheerschmidt and M. Werner, Phys. Status Solidi A **202**, 2368 (2005).
[100]K. Yang, G. H. Schwuttke, and T. F. Ciszek, J. Cryst. Growth **50**, 301 (1980).
[101]B. L. Sopori and A. Baghdadi, Sol. Cells **1**, 237 (1980).
[102]J. Chen, T. Sekiguchi, D. Yang, F. Yin, K. Kido, and S. Tsurekawa, J. Appl. Phys. **96**, 5490 (2004).
[103]T. Buonassisi, G. Hahn, A. M. Gabor, J. Schischka, A. A. Istratov, M. D. Pickett, and E. R. Weber, *20th European Photovoltaic Solar Energy Conference and Exhibition* (WIP-Munich, Barcelona, Spain, 2005).
[104]T. Buonassisi, A. A. Istratov, M. D. Pickett, M. A. Marcus, T. F. Ciszek, and E. R. Weber, Appl. Phys. Lett. **89**, 042102 (2006).
[105]M. Werner, K. Scheerschmidt, E. Pippel, C. Funke, and H. J. Moeller, *Carbon in multicrystalline ribbon-silicon for solar cell application* (Institute of Physics, Bristol, United Kingdom, 2004), p. 65.
[106]H. J. Möller, C. Funke, M. Rinio, and S. Scholz, Thin Solid Films **487**, 179 (2005).
[107]B. Sopori and W. Chen, J. Cryst. Growth **210**, 375 (2000).
[108]J. Isenberg, J. Dicker, S. Riepe, C. Ballif, S. Peters, H. Lautenschlager, R. Schindler, and W. Warta, *29th IEEE Photovoltaic Specialists Conference* (IEEE, Piscataway, NJ, 2002), p. 198.
[109]K. Nakayashiki, V. Meemongkolkiat, and A. Rohatgi, IEEE Trans. Electron Devices **52**, 2243 (2005).
[110]V. Kveder, M. Kittler, and W. Schröter, Phys. Rev. B **63**, 115208 (2001).
[111]D. Macdonald and A. Cuevas, Phys. Rev. B **67**, 075203 (2003).
[112]C. P. Foy, J. Phys. C **15**, 2059 (1982).
[113]J. Coutinho, O. Andersen, L. Dobaczewski, K. B. Nielsen, A. R. Peaker, R. Jones, S. Oberg, and P. R. Briddon, Phys. Rev. B **68**, 184106 (2003).
[114]T. S. Fell and P. R. Wilshaw, J. Phys. IV **01**, C6-211 (1991).
[115]B. L. Sopori, R. W. Gurtler, and I. A. Lesk, Solid-State Electron. **23**, 139 (1980).
[116]C. Donolato, J. Appl. Phys. **84**, 2656 (1998).
[117]M. Rinio, S. Peters, M. Werner, A. Lawerenz, and H.-J. Möller, Solid State Phenom. **82–84**, 701 (2002).
[118]N. Usami, R. Yokoyama, I. Takahashi, K. Kutsukake, K. Fujiwara, and K. Nakajima, J. Appl. Phys. **107**, 013511 (2010).
[119]N. Stoddard, R. Sidhu, G. Rozgonyi, I. Witting, and P. V. Dollen, *Third International Workshop on Crystalline Silicon Solar Cells* (NTNU/SINTEF, Trondheim, Norway, 2009).
[120]T. Buonassisi, A. A. Istratov, M. D. Pickett, J. P. Rakotoniaina, O. Breitenstein, M. A. Marcus, S. M. Heald, and E. R. Weber, J. Cryst. Growth **287**, 402 (2006).
[121]M. Trushin, W. Seifert, O. Vyvenko, J. Bauer, G. Martinez-Criado, M. Salome, and M. Kittler, Nucl. Instrum. Methods Phys. Res. B **268**, 254 (2010).
[122]A. A. Giardini, Am. Mineral. **43**, 249 (1958).
[123]T. Iwaki and T. Koizumi, Exp. Mech. **29**, 295 (1989).
[124]E. D. Palik, *Handbook of Optical Constants of Solids* (Academic, San Diego, CA, 1998), p. 529.

DISCLAIMER
This document was prepared as an account of work sponsored by the United States Government. While this document is believed to contain correct information, neither the United States Government nor any agency thereof, nor The Regents of the University of California, nor any of their employees, makes any warranty, express or implied, or assumes any legal responsibility for the accuracy, completeness, or usefulness of any information, apparatus, product, or process disclosed, or represents that its use would not infringe privately owned rights. Reference herein to any specific commercial product, process, or service by its trade name, trademark, manufacturer, or otherwise, does not necessarily constitute or imply its endorsement, recommendation, or favoring by the United States Government or any agency thereof, or The Regents of the University of California. The views and opinions of authors expressed herein do not necessarily state or reflect those of the United States Government or any agency thereof or The Regents of the University of California. Ernest Orlando Lawrence Berkeley National Laboratory is an equal opportunity employer.